alloys

MDPI

Article

Microstructure, Room and High-Temperature Mechanical Properties of As-Built PBF-LB W360 Hot Forming Steel Alloy

Morgane Mokhtari [1,*], Robin Guillon [1], Fábio J. P. Simões [2], Tiago Marques [3], Artur Mateus [4], Yannick Balcaen [1] and Joël Alexis [1]

[1] LGP, UTTOP, University of Toulouse, 65000 Tarbes, France; robin.guillon@uttop.fr (R.G.); yannick.balcaen@uttop.fr (Y.B.); joel.alexis@uttop.fr (J.A.)
[2] CDRSP—Center for Rapid and Sustainable Product Development, Polytechnic of Leiria, 2430-028 Marinha Grande, Portugal; fabio.simoes@ipleiria.pt
[3] Moldetipo, Lda, 2430-091 Marinha Grande, Portugal
[4] ISISE—The Institute for Sustainability and Innovation in Structural Engineering, Engineering Department, University of Coimbra, 3030-788 Coimbra, Portugal; artur.mateus@dec.uc.pt
* Correspondence: morgane.mokhtari@uttop.fr

Abstract

To produce increasingly efficient tools with optimized geometry, additive manufacturing is a suitable solution. However, tool steels, due to their high amount of carbon and hardening elements, may be unweldable and therefore difficult to produce using additive manufacturing methods that employ melting. W360 is a hot-forming alloy, and, in this study, it was produced through laser powder bed fusion (PBF-LB). The microstructure and mechanical properties were evaluated on as-built netshape PBF-LB samples. Despite the presence of many alloying elements, this alloy was not sensitive to cracks, and very good results from the defect analysis (defect surface density < 0.2%) were achieved. Microstructure and hardness are homogeneous in the sample except in the last layer due to an upskin effect. As-built netshape samples exhibit very promising mechanical properties up to 400 °C, which could be further improved by heat treatments.

Keywords: additive manufacturing; laser powder bed fusion; hot-forming steel; high temperature tensile tests; mechanical properties

1. Introduction

Recently, to avoid machining and assembly steps, additive manufacturing (AM) has emerged as a promising solution. It can produce complex parts directly from computer-aided design, a capability indispensable to modern industry. Among all metal AM techniques, laser powder bed fusion (PBF-LB) is the most studied and mature technique [1]. Compared to Laser Directed Energy Deposition (DED-LB), PBF-LB enables very accurate, topologically optimized components to be obtained, while DED provides a high deposition rate, which is more suited for larger components and repair applications [2]. Moreover, PBF-LB is a mature technology and enables the production of more efficient redesigned parts, which are required in industrial contexts [1,2].

PBF-LB can produce standard alloys such as aluminum alloys [3], titanium alloys [4,5], nickel-based superalloys [6], steels [7–9] and some specific alloy compositions optimized for AM processes [10–12]. However, due to the high cooling rate (up to 10^6 K/s) and steep thermal gradient imposed during the process, non-weldable alloys are difficult to

Check for updates

Academic Editors: Pavel Krakhmalev and Arne Mattias Thuvander

Received: 22 April 2026
Revised: 9 June 2026
Accepted: 13 July 2026
Published: 24 July 2026

Copyright: © 2026 by the authors. Licensee MDPI, Basel, Switzerland. This article is an open access article distributed under the terms and conditions of the Creative Commons Attribution (CC BY) license.

produce using this technique [13]. Indeed, very hard alloys such as tool steel are often crack-sensitive, and the presence of cracks will hinder the quality of the final part [14–16].

W360 is a novel hot-forming steel alloy sold as a conventional raw product (sheet, rod, etc.) and as a powder. This material is said to have high toughness, fair ductility, good wear resistance, fair machinability, good hardness at elevated temperature, and good thermal conductivity [17]. Its microstructure in the conventional manufacturing route consists mainly of the BCC/BCT martensitic phase, with a small amount of retained austenite [18–20]. It has been shown that the recommended heat treatment with multiple tempering cycles refines martensite laths and grains, leading to high hardness (696 HV0.2) and impact toughness (AK_U = 21.3 J) [18]. Despite the high hardness, a ductile Charpy impact test fracture mode was noticed. Wear properties and autofrettage processing were analyzed and compared with those of more common materials, such as H10, H13, and 1.2344 steels, as well as Unimax, which showed promising properties [18–20]. Another study reports the evaluation of nitriding a W360 hot forging die for the production of an engine valve. Three critical wear mechanisms were identified (plastic deformation, thermo-mechanical fatigue, and abrasive wear) [21]. W360 heat treatment was numerically investigated. For most cooling rates (until 3 K/s), martensite and a small amount of retained austenite were obtained. The residual stresses after hardening were compressive in the subsurface layer, and the depth of this layer increased with higher cooling rates. However, rapid changes in thermal strains may lead to microcracks [22].

All the above-mentioned studies deal with conventional forms of W360 products. In all these studies, W360 is either compared to other materials or used as an example to investigate new numerical methods. More recently, a couple of papers concerning W360 produced by PBF-LB were also published. For example, variations in mechanical properties depending on the applied heat treatment were studied [23–25]. Based on the microstructure, ferrite with a small amount of residual austenite was detected after stress relief treatment. Additional tempering steps enabled the precipitation of hardening $M_{23}C_6$, M_7C_3 and M_6C phases in the ferritic matrix, resulting in a hardness of 630–670 HV, a tensile yield strength of around 1700 MPa, an ultimate tensile stress of 2100–2300 MPa and an elongation at break of around 1.5–3.8% [23–25]. However, the as-built state is almost uninvestigated. The evolution of microstructure on as-built DED-LB, as-quenched, and after tempering was studied, and the martensite phase was found in all conditions, even after tempering for 3 h at 540 °C [26]. They show that quenching increases the number of carbides, and tempering enables a homogeneous microstructure of tempered martensite while retaining carbides.

Therefore, there is a lack of literature considering the investigation of the microstructure and mechanical properties of as-built W360. In this way, this paper aims to address this issue by investigating the material health, microstructure, and room- and elevated-temperature mechanical properties of W360 manufactured by PBF-LB.

2. Materials and Methods

2.1. Materials

W360 hot tool steel powder supplied by Böhler (Kapfenberg, Germany) is purchased for this study. Powder composition provided by the supplier and bulk composition measured by a Foundry Master spark optical emission spectrometer (Oxford instruments, Abingdon-on-Thames, UK) are listed in Table 1.

Powder particles are spherical, with a narrow particle size distribution (D10 = 21.3 ± 0.7 µm, D50 = 32.0 ± 0.8 µm, and D90 = 45.8 ± 0.9 µm), consistent with the values reported by the supplier [17].

Table 1. Powder and bulk compositions (weight%) [27].

	Fe	C	Si	Mn	Cr	Mo	V	O	N	S	W
Powder (Böhler) [17]	Bal.	0.5	0.2	0.25	4.5	3	0.55	/	/	/	/
As-built PBF-LB (exp)	91.05 ± 0.02	0.459 ± 0.004	0.181 ± 0.003	0.207 ± 0.002	4.42 ± 0.02	2.83 ± 0.01	0.582 ± 0.002	/	/	<0.005	0.128 ± 0.004

Samples were produced by the PBF-LB process using a Trumpf TruPrint 1000 machine (Ditzingen, Germany) (power up to 200 W) equipped with a 30 µm diameter laser beam. The manufacturing parameters are displayed in Table 2 and were obtained from a preliminary study based on parameters derived from the manufacturer's recommendations for AISI316L. In the building chamber, the oxygen level was maintained below 3 ppm. The build plate was not preheated because this equipment does not have this capability. Core material was scanned using a chess strategy (block length of 3.96 mm and a pattern shift from layer to layer of 2.7648 mm in the X direction and 2.9769 mm in the Y direction), with a 45° rotation between layers. The recoater travels in the X direction. In the following sections, the building direction corresponds to the Z-axis, while the XY plane corresponds to the scanning plane. To analyze defects, microstructure and hardness, block samples ($14 \times 14 \times 10$ mm^3) were built. For room temperature tensile tests, dog-bone-shaped specimens were vertically built. For high-temperature tensile tests, cylindrical specimens were vertically built. For Charpy impact tests, ASTM E23 reduced-size 2.5×10 mm (55 mm length) bars were vertically and horizontally built. Then they were V-broached. No further heat treatments were applied. An illustration of these explanations is provided in Figure 1.

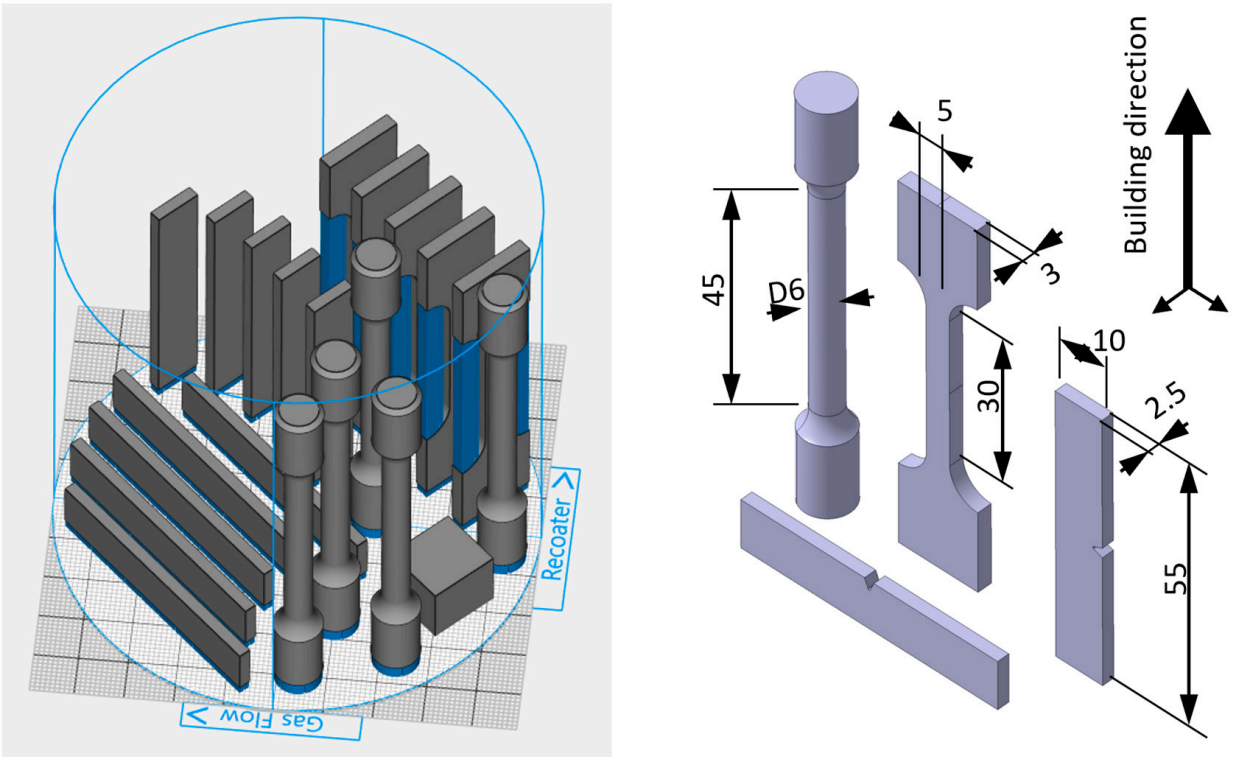


Figure 1. Schematic representation of building plate during the process (**left**), Schematic representation of mechanical test specimens. Lengths are given in mm (**right**).

Table 2. PBF-LB manufacturing parameters.

Position	Laser Power (P) (W)	Laser Scanning Speed (v) (mm/s)	Layer Thickness (µm)	Hatching Distance (µm)
Core	120	700	20 µm	90 µm
Downskin	30	460	20 µm	30 µm
Contouring	80	500	Not Applicable	Not Applicable
Upskin	120	700	20 µm	90 µm

2.2. Methods

2.2.1. Defect Analysis and Microstructural Characterization

For defect analysis and microstructural characterization, optical micrography was acquired using an Olympus PMG3 optical microscope (Evident, Tokyo, Japan) on sample cross-sections. For higher-magnification imaging, a ZEISS EVO HD15LS scanning electron microscope (SEM) (Zeiss France, Paris, France) equipped with an energy-dispersive X-ray (EDX; Oxford Instruments, Abingdon-on-Thames, UK, X-Max 50 mm^2) detector was employed. The sample preparations required initial mechanical polishing steps using P4000-grit papers (Buehler, Leinfelden-Echterdingen, Germany) and an automatic mechanical polisher (Mecatech 334, Presci, Eybens, France). Then, colloidal diamond solutions (3 µm, 1 µm) and oxide polishing solutions (OPS) were used. In order to reveal the microstructure, samples were etched by immersing them for 10 s in Nital etching solution (97 mL ethanol, 3 mL nitric acid). Image J analysis software (Fiji version)) was used for quantitative image analysis [28]. For phase quantitative analysis, XRD spectra were recorded at the ID22 beamline of ESRF (Grenoble, France), utilizing a 1×1 mm^2 X-ray beam with a wavelength of $0.35431132 \pm 0.00000324$ Å and a Dectris Eiger 2×2 m-w CdTe detector equipped with nine Si (111) crystals (Dectris USA, Philadelphia, PA, USA) [29–31]. The samples were scanned with a step size of 0.0001° at 251 rpm, resulting in a total acquisition time of 16 min. Results were analyzed with the ICCD database.

2.2.2. Mechanical Characterization

Room-temperature hardness indents were performed using the Zwick/Roell ZHV2.5 equipment (Zwick, Ulm, Germany) with a Vickers indent with two different loads: 10 kg (HV10) (macrohardness), 0.2 kg (HV0.2) (microhardness). For microhardness testing, a 10 kg load was applied to a bulk sample. The result is the average value of 30 measurements. For microhardness measurements, at least 300 indentations were recorded in each plane. An electromechanical Instron 5892 tensile machine was used to perform tensile tests. Deformation rate was controlled with a crosshead displacement mode of 2 mm/min. This implies a strain rate of around 2×10^{-3} s^{-1} on the sample. For room-temperature tests, dog-bone-shaped specimens ($5 \times 3 \times 35$ mm^3) were used, while for high-temperature tests, cylindrical samples (diameter 6 mm, gauge length 45 mm) were printed. Prior to tensile testing, to remove excessive surface roughness and improve cross-section measurement accuracy, the surface of the specimens was polished with P600 SiC paper (Buehler, Leinfelden-Echterdingen, Germany). The strain of samples tested at room temperature was measured using a digital video extensometer. The elastoplastic transition was defined as the stress corresponding to a plastic strain of 0.2%. High-temperature tensile tests were performed at 300 °C and 400 °C using an SF-16 furnace (Instron, Norwood, MA, USA). Tests were started after temperature stabilization, and strain was measured using a 25 mm gauge-length extensometer (I3448-025M-020, Instron, Norwood, MA, USA). Charpy impact tests were performed on as-built samples with a 2.5×10 mm V-notched geometry, using a Zwick HIT 50P pendulum (Zwick, Ulm, Germany) with a 50 J capacity at room temperature.

3. Results and Discussion

3.1. Defect Analysis

For the defect analysis, the cross-sections of the samples were observed. The result of this investigation is shown in Figure 2. Several pores can be observed in the bulk and are also aligned with the sample edge. The contouring strategy may explain the one near the sample edge, which is aligned along the building direction [32]. In the literature [23–25], the buildplate was preheated to 400 °C to avoid large cracking issues. Therefore, this study shows that preheating produces acceptable results. In addition, a second kind of defect can be observed: cracks. In the upper region, especially in the last layer, microcracks are evident. This defect is well known in tool steels (such as AISI M2 and AISI M50) with compositions close to W360. Cracking can be avoided by reducing the thermal gradient by pre-heating the build plate [16,33–35]. The last layer has a different thermal history from the bulk area, which may explain the cracks. However, the defect location may not make them harmful because they will be removed by surface machining.

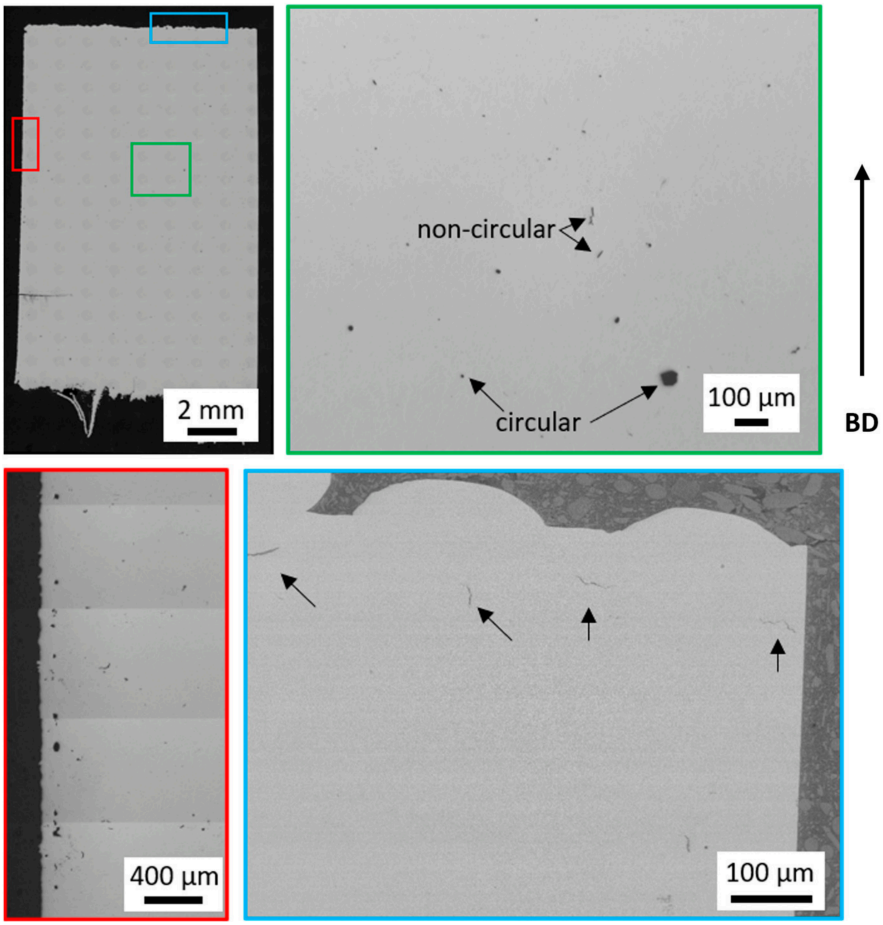


Figure 2. Optical micrographs of the sample (polished, no etching) half XZ plane. An arrow indicates the building's direction (BD). Small arrows highlight cracks in the upper layer. High magnification images of some areas are also provided.

A quantitative analysis was also performed. On the half XZ plane (cf. Figure 2), a surface density of 99.82% was measured. Then, on each plane, a total area of 22 mm^2 was carefully analyzed (XY, XZ, YZ). It corresponds to approx. 10% of the total plane surface. On each plane, several optical images were acquired in different areas where the pore density is important. Due to the micrography resolution, defect diameters lower than 0.7 µm were not considered. Statistical results indicate a surface density of 99.86 ± 0.06%, consistent

with the literature [23–25], and an average defect diameter of 5 ± 6 µm, indicating excellent material health. Defects were then divided into two categories: circular (circularity > 0.9) or non-circular ones. Indeed, sharp defects can lead to stress concentrations, which can favor crack propagation. Defect size distribution and circularity are plotted in Figure 3. Most circular defects (99%) have an average diameter lower than 15 µm, although this is the case for only 80% of non-circular defects. Another difference is defect number: 647 non-circular vs. 1092 circular, but non-circular defects have a higher equivalent diameter and represent a higher surface density, 0.03% vs. 0.02%. In conclusion, PBF-LB classical defects could not be avoided. However, the low porosity and limited defect diameter are consistent with results reported in the PBF-LB literature s [23–25].

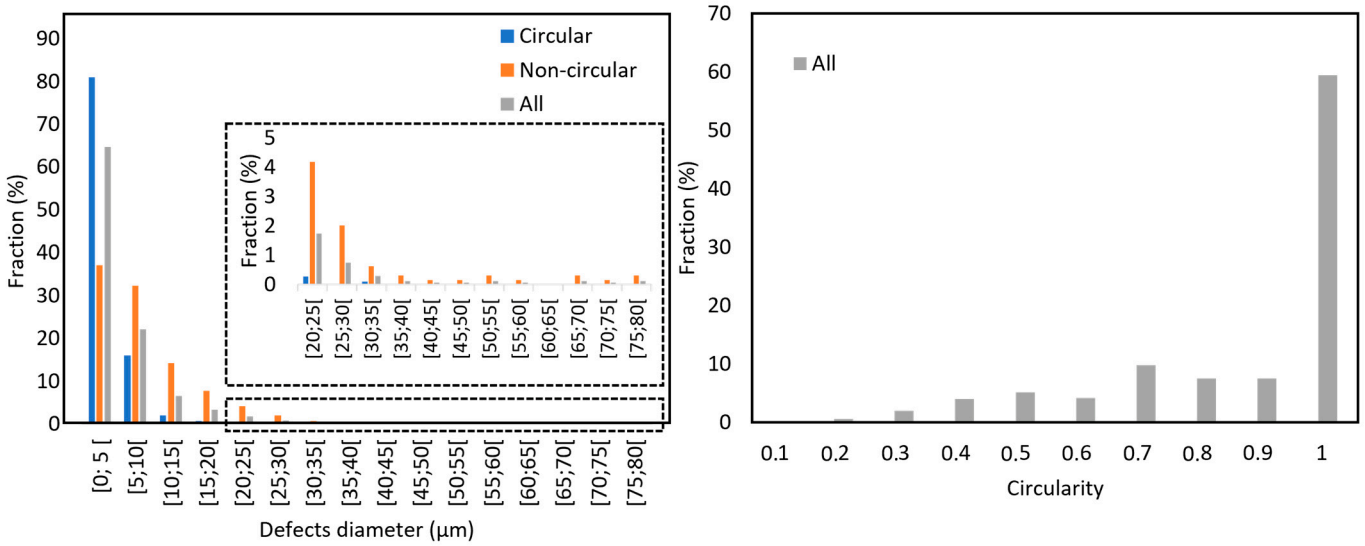


Figure 3. Defect size distribution (zoom of defect diameters [25;80] inside the dash line) (**left**). Defects circularity distribution (**right**).

3.2. Material Microstructure

Macrostructure was investigated using an optical microscope (Figure 4, top). A typical PBF-LB melt pool is visible. However, the top layer is not similar to the sample's core, which means there is a difference in composition or microstructure in this last layer. Nothing in the process accounts for such a large compositional difference between the last and previous layers, which explains the high hardness variation. Therefore, this difference cannot be attributed to a composition gradient. This layer has a different thermal history with no remelting and no subsequent heat treatment due to the construction. It can lead to microstructure variations between the core and the last layer.

To investigate laser–matter interactions, melt pool dimensions were measured in two planes on the last layer. The results are presented in Table 3. Keyhole mode is considered for a height/half-width ratio higher than 2.5. Melt pools are isotropic. The height-to-width measured ratio implies a laser-matter interaction in a keyhole mode [1,36]. This mode is associated with a high energy density and is not favored because it can generate keyhole porosity [1,36]. In PBF-LB, the conduction mode is preferable to limit porosity formation; however, in this specific study, the keyhole is not harmful for production.

At higher magnification (Figure 4, bottom), a typical PBF-LB cellular microstructure was observed inside the melt pool. The literature also reports cellular or needle-like structures for martensitic steel [34,37]. Cell size is not homogeneous in the sample. Some heterogeneities are observed near the melt pool boundaries or the sample surface. Cell size is linked to cooling rates during solidification. Therefore, different cell sizes imply different cooling rates [1]. The average cell size is 0.7 ± 0.3 µm, within the range reported in the

literature [38]. Cell walls and cell cores should show compositional differences; however, due to cell size, it was not possible to assess the compositional gradient using SEM-EDX. However, at higher magnification, needle-like or lath-like features, typical of martensitic microstructures, were observed in the cell core. The results differ from [24], where no cellular microstructure was found. However, the temperature during production was kept at 400 °C, above Ms, which may explain the difference.

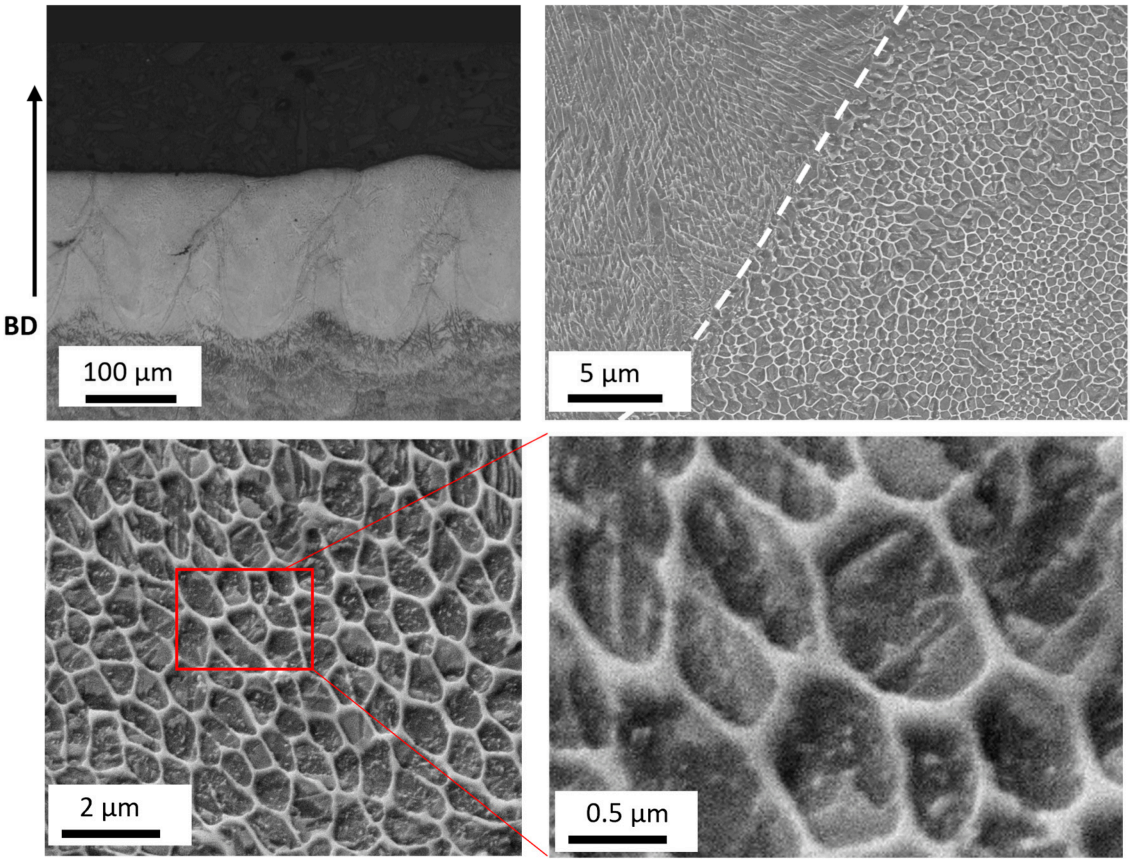


Figure 4. The arrow corresponds to the building direction. (**left**) Optical micrography of macrostructure. Melt pool boundaries are visible. (**right**) SEM image of microstructure. Cellular microstructure is visible. The melt pool boundary is highlighted by a dashed line. (**bottom**) Highlight of cellular microstructure. Martensite laths are visible inside the cells.

Table 3. Melt pool dimensions [27]. XZ and YZ correspond to two perpendicular cross-sections, both parallel to the building direction.

Melt Pool Dimensions	XZ Plane	XY Plane
height (µm)	190 ± 20	186 ± 15
width (µm)	86 ± 9	96 ± 10
Melt pool aspect ratio [36]	~4.4	~3.9

To investigate the crystallographic structure, XRD patterns were acquired (Figure 5). W360 is a martensitic steel. Therefore, the BCC or BCT iron phase was detected. This high-angular-resolution analysis detects only one peak. Therefore, it suggests that only martensite or tempered martensite is present (no coexistence of ferrite and martensite in the bulk). However, retained austenite was detected, which is common for martensitic steel produced by PBF-LB [35,39–41]. Our result is consistent with previous studies on PBF-LB W360 [23,24]. In a previous study [23], a BCC phase was considered due to the

preheating plate at 400 °C during the process and stress relief at 690 °C. In all cases [23,24], the iron carbide phase was not detected. However, chromium carbides were detected after tempering. This residual austenite shows peak deviation from pure iron due to the high amount of elements in solid solution. The relatively high martensite start temperature (~280 °C) [17] suggests residual austenite content of less than 1%.

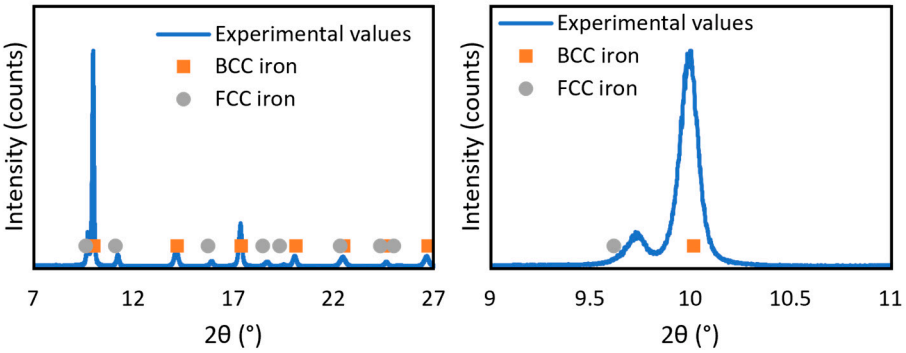


Figure 5. XRD spectra, full (**left**), zoom (**right**).

3.3. Mechanical Properties

In this part, hardness and impact toughness are investigated at room temperature and tensile properties are presented up to 400 °C.

3.3.1. Hardness Tests

Macro- and micro-hardness measurements were performed, and the results are displayed in Table 4. Indentation tracks (more than 200 indentations on each plane) were performed for micro-hardness, and homogeneous hardness for both width and height was measured. A high as-built macro-hardness slightly below the value expected after further heat treatment, comprising solution treatment and tempering (590–630 HV) from the powder supplier [17], which was measured, is very promising. A very low anisotropy between vertical and horizontal planes was noticed; therefore, an isotropic macroscopic mechanical behavior is expected. In the first layer, the higher value can be explained by an upskin effect. This first layer was neither remelted nor tempered by thermal reloading, and it was built using the same parameters as the core material. Therefore, core materials correspond to tempered martensite, while the last layer corresponds to as-built martensite. The supplier data suggest that heat treatment may slightly improve the global hardness value, while the hardness of heat-treated samples reported in the literature is consistent with ours [23–25].

Table 4. Hardness measurements [27].

	XY Plane	XZ Plane	YZ Plane
Macro-hardness		550 ± 30 HV10	
Micro-hardness bulk	678 ± 41 HV0.2	648 ± 31 HV0.2	644 ± 47 HV0.2
Micro-hardness top layer	/	819 ± 54 HV0.2	

3.3.2. Charpy Impact Tests

Tests were performed on as-built samples at room temperature (Table 5). Horizontal samples show lower values than vertical ones. Vertical samples almost reached the properties claimed by the supplier after heat treatment. Figure 6 displays SEM fractographies at different magnifications for both vertically and horizontally built samples. At a macro scale, a brittle behavior is observed. However, at higher magnification, a mix of ductile

and brittle failure is observed, accompanied by small dimples. Crack propagation seems to be influenced by microstructure features, which at this scale could be grain structure. Wrought heat-treated W360 exhibits comparable ductile behavior [18]. Therefore, ductility may be increased after heat treatment in our case. With other hot-tool steels, the values are slightly higher, consistent with conventional material properties [18,42].

Table 5. As-built impact toughness values [27].

	As-Built Vertical Samples	As-Built Horizontal Samples
Sample geometry	ASTM V-notch reduced size 2.5 × 10 mm	
Impact toughness	9.52 ± 1.08 J/cm^2	7.79 ± 1.06 J/cm^2

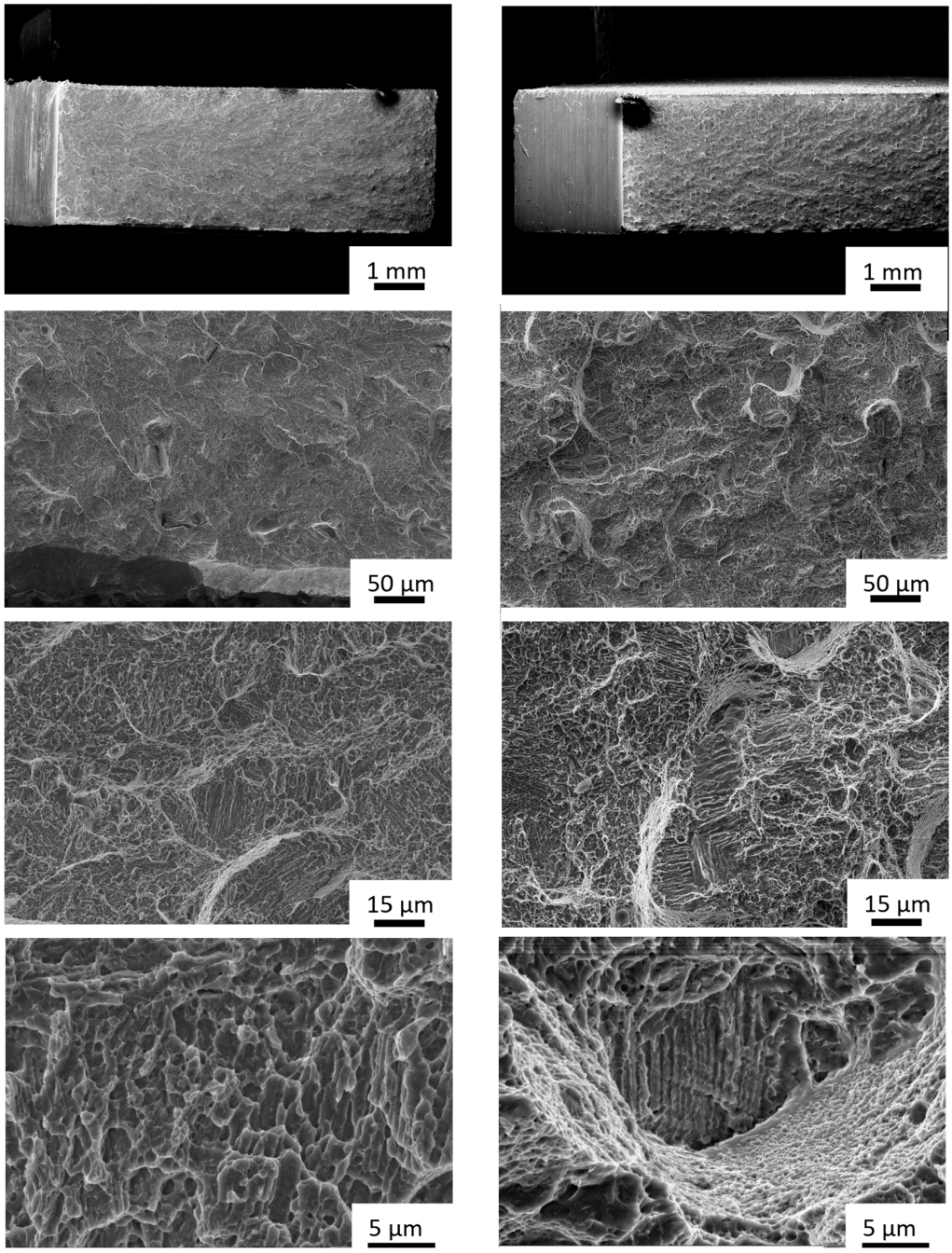


Figure 6. SEM observations at different magnifications after failure.

3.3.3. Tensile Tests

On as-built samples, tensile properties were investigated at room and higher temperatures. At least two tests were performed for each condition. Engineering stress–strain curves are plotted in Figure 7. Yield stress (YS), ultimate tensile strength (UTS), and elongation at break (A%) values were determined from these plots. The results are summarized in Table 6. First, one can observe good reproducibility and rather poor ductility at room temperature. Ductility does not improve at higher temperatures. Though the yield strength and ultimate tensile strength are high, they are slightly lower than those reported by the supplier (YS = 1500–1670 MPa, UTS = 1970–2010 MPa, A% = 6.6–8.1%) for the heat-treated sample [17]. Given the as-built properties, one can expect that PBF-LB samples will achieve the targeted properties after heat treatment. Regarding high-temperature tensile properties, they are maintained at least up to 400 °C, consistent with the constant hardness value up to 550 °C reported in [17]. Tensile properties (YS and UTS) values are in the range of as-built H13 steel on a non-preheated building plate [16] but are lower than those of W360 after heat-treatment [23–25].

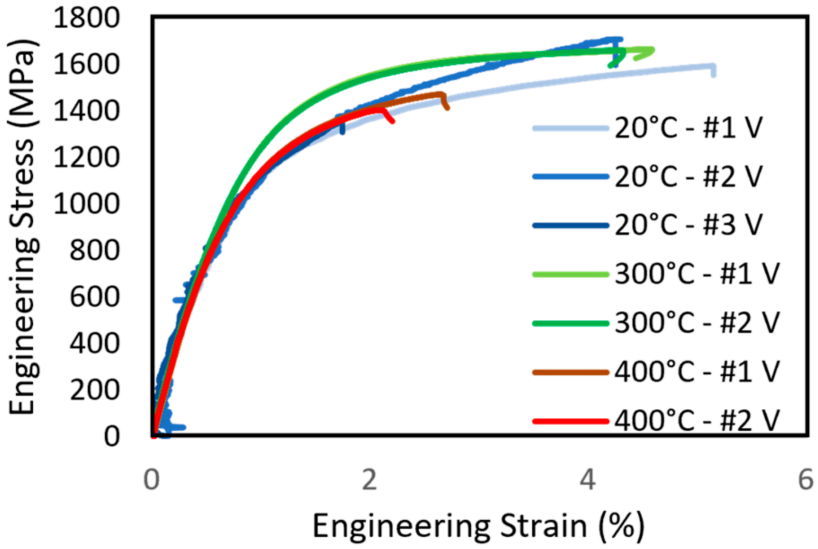


Figure 7. Engineering stress–strain curves of vertically (V) built samples at room temperature, at 300 °C and 400 °C.

Table 6. As-built tensile properties extracted from Figure 6 curves.

Samples	YS (MPa)	UTS (MPa)	A%
As-built vertical (room temperature)	1189 ± 52	1552 ± 52	3.7 ± 1.6%
As-built vertical (T = 300 °C)	1235 ± 54	1665 ± 2	4.6 ± 0.4%
As-built vertical (T = 400 °C)	1141 ± 6	1439 ± 48	2.4 ± 0.4%

Figure 8 shows SEM observations after failure at different magnifications for the different tensile test temperatures. On room-temperature fracture surfaces, grain-structure features are clearly noticeable, and higher magnification allowed martensite laths to be identified. These flat areas are typical of a mixed (ductile and brittle) fracture mode. For samples tested at 300 °C and 400 °C, the fracture surfaces exhibit fewer brittle areas and greater overall waviness. At high magnification, dimples are easily detected.

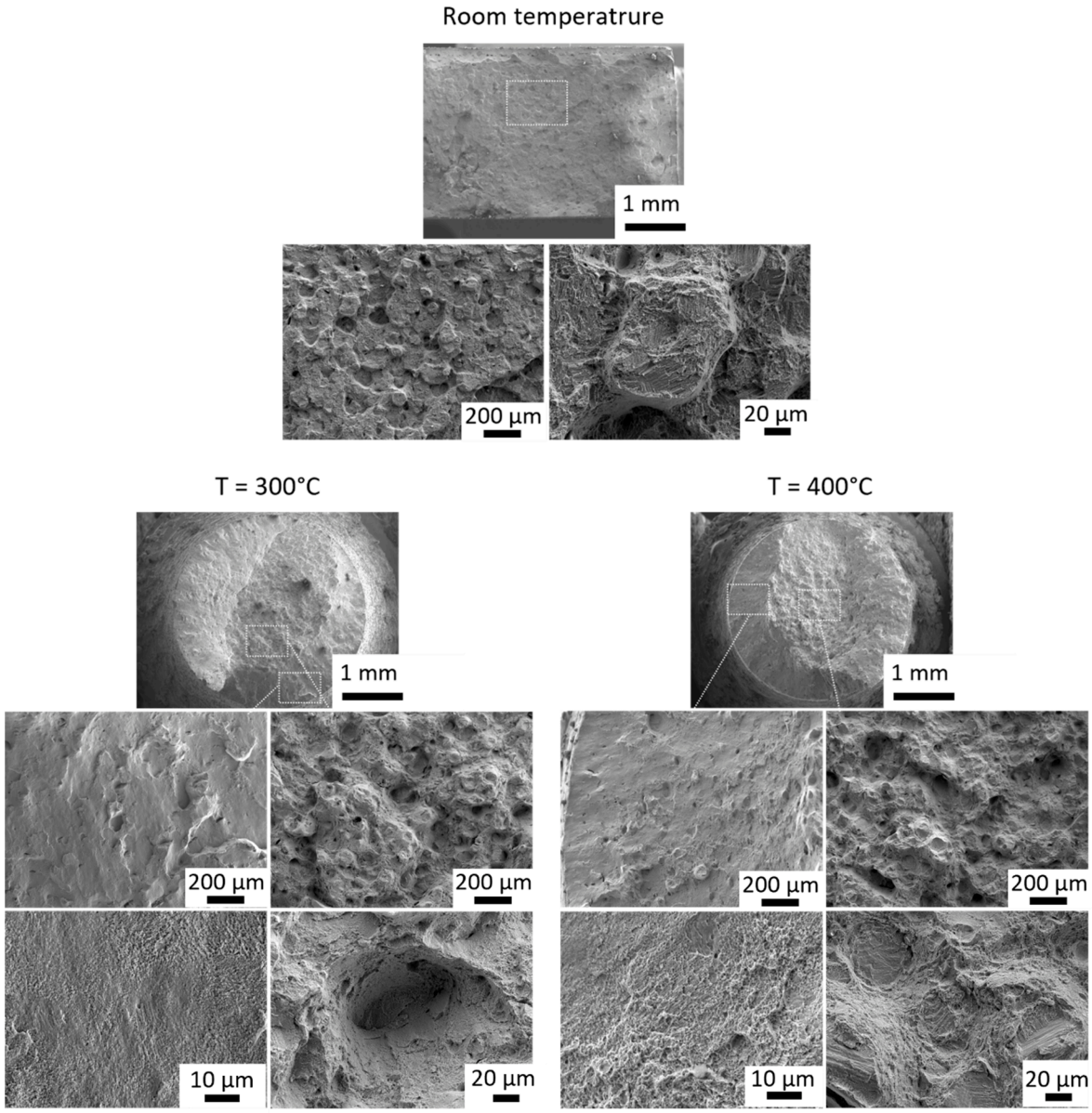


Figure 8. SEM observations of tensile samples' fracture surfaces. White frames correspond to high magnification images position.

3.4. Discussion on Process-Microstructure-Properties Relationships

Process parameters imply an area energy density AED (P/(v.d)) with d focal beam diameter) [43] of 5.7 MJ/m^2. This value is clearly above 1 MJ/m^2, the minimum required to transition from conduction mode to keyhole mode [44]. According to Huang et al. [43], at this energy density, a quasi-stable keyhole mode is achieved, thereby limiting the formation of keyhole pores. The cooling rate (R) may be estimated from $\lambda = 83.R^{-0.3}$ (a constant for low-alloy steel [45]) where λ is the cell size. A value of R = 8.2 10^6 K^{-1} is consistent with values reported for PBF-LB methods [1].

Even if large defects are present (up to an equivalent diameter of 77 µm), it is consistent with the literature, where a remarkable number of defects with an equivalent diameter in the range 10–100 µm and a lower density than ours were reported [24]. However, our tensile properties are lower, which cannot be attributed to a lower density. Therefore, it can be explained by the use of a post-heat treatment in the literature [24]. Reference [24] shows that fatigue crack initiation occurs in a large noncircular defect (attributed to lack of fusion); therefore, the large noncircular defect detected may reduce fatigue properties.

4. Conclusions

This study investigates the microstructure and mechanical properties of as-built PBF-LB W360. Several conclusions can be drawn:

- Despite the lack of building plate preheating, a high density (>99.8%) was obtained. However, some defects (cracks, pores) were detected. Most of them are related to the scanning strategy (contouring and upskin) and will be removed during the machining of the final part. Therefore, there is no need to build a plate preheating system to achieve proper material health.
- A typical cellular microstructure with very thin cells (around 0.7 μm) was observed, leading to the evaluation of the cooling rate at 8.2 10^6 K^{-1}. For deeper analysis, TEM observations should be performed in the future to obtain more details, specifically on element segregation.
- As-built net-shape mechanical properties were measured. Tensile and impact properties are already high without heat treatment. They are not meeting the expected values after heat treatment and machining, but are very promising. These high mechanical properties are maintained at least up to 400 °C.

In conclusion, W360 is a very promising material for hot-forming applications. Even if as-built mechanical properties are high, there is still room for improvement; mechanical properties can be enhanced by heat treatment. Therefore, these should be designed to exploit the specific as-built cellular microstructure, and the resulting mechanical properties should be measured.

Author Contributions: Conceptualization, J.A., Y.B., M.M., A.M., T.M. and F.J.P.S.; investigation, R.G., Y.B., M.M., A.M., T.M. and F.J.P.S.; writing—original draft preparation, R.G., Y.B., M.M. and J.A.; writing—Review & Editing, R.G., Y.B., M.M., F.J.P.S. and J.A.; visualization, R.G., Y.B., M.M. and J.A.; project administration, J.A. and A.M. All authors have read and agreed to the published version of the manuscript.

Funding: This work was supported by the Interreg-SUDOE Program, by the ADDITOOL project [grant number SOE4/P1/F1006]. Fábio J. P. Simões ackowledges Fundação para a Cieência e a Tecnologia (FCT) for its financial support via the project CDRSP Funding (DOI: 10.54499/UID/04044/2025) and ARISE funding (DOI: 10.54499/LA/P/0112/2020).

Data Availability Statement: The original contributions presented in this study are included in the article. Further inquiries can be directed to the corresponding author.

Acknowledgments: The authors acknowledge Jade Pecune and Nathalie Aubazac for their technical support with sample preparation, hardness measurement and SEM observations, respectively. We thank Geoffrey Baratte for participating in the experimental data collection. The authors also thank reconstruction and Pierre Diaz from ESTIA for leading the project and all people in the Additool project involved in the MOLDETIPO demonstrator. Additional information on this project can be found on the dedicated website [27]. European Synchrotron Radiation Facility (ESRF) for providing access to facilities under Proposal Number MA-5643, and we would like to thank all the staff at the ID11 Beamline.

Conflicts of Interest: Author Tiago Marques was employed by the company Moldetipo. The remaining authors declare that the research was conducted in the absence of any commercial or financial relationships that could be construed as a potential conflict of interest.

References

1. DebRoy, T.; Wei, H.L.; Zuback, J.S.; Mukherjee, T.; Elmer, J.W.; Milewski, J.O.; Beese, A.M.; Wilson-Heid, A.; De, A.; Zhang, W. Additive Manufacturing of Metallic Components—Process, Structure and Properties. *Prog. Mater. Sci.* **2018**, *92*, 112–224. [CrossRef]
2. Blakey-Milner, B.; Gradl, P.; Snedden, G.; Brooks, M.; Pitot, J.; Lopez, E.; Leary, M.; Berto, F.; Du Plessis, A. Metal Additive Manufacturing in Aerospace: A Review. *Mater. Des.* **2021**, *209*, 110008. [CrossRef]

3. Kotadia, H.R.; Gibbons, G.; Das, A.; Howes, P.D. A Review of Laser Powder Bed Fusion Additive Manufacturing of Aluminium Alloys: Microstructure and Properties. *Addit. Manuf.* **2021**, *46*, 102155. [CrossRef]
4. Tshephe, T.S.; Akinwamide, S.O.; Olevsky, E.; Olubambi, P.A. Additive Manufacturing of Titanium-Based Alloys—A Review of Methods, Properties, Challenges, and Prospects. *Heliyon* **2022**, *8*, e09041. [CrossRef] [PubMed]
5. Alipour, S.; Moridi, A.; Liou, F.; Emdadi, A. The Trajectory of Additively Manufactured Titanium Alloys with Superior Mechanical Properties and Engineered Microstructures. *Addit. Manuf.* **2022**, *60*, 103245. [CrossRef]
6. Saleh, B.; Fathi, R.; Zhao, L. Additive Manufacturing of Nickel Superalloys: A Critical Review of Recent Advances and Future Perspectives. *Appl. Mater. Today* **2026**, *48*, 103051. [CrossRef]
7. Zadi-Maad, A.; Rohib, R.; Irawan, A. Additive Manufacturing for Steels: A Review. In *IOP Conference Series: Materials Science and Engineering*; IOP Publishing: Bristol, UK, 2018; Volume 285, p. 012028. [CrossRef]
8. Manikandan, P.; Venkatesan, K. A Review of Post-Processing Techniques for Additive Manufactured Stainless Steel: Enhancing Surface Quality and Mechanical Properties. *Proc. Inst. Mech. Eng. Part L J. Mater. Des. Appl.* **2026**, 14644207251413481. [CrossRef]
9. Abdelaal, A.F.; Chakrobarty, A.; Sakib, M.N.; Arka, A.M.; Sabuz, E.H. Porosity, Residual Stress, Wear Properties and Impact Toughness of Additively Manufactured Low-Alloy Steel: A Review. *Next Mater.* **2025**, *9*, 101288. [CrossRef]
10. Guo, Q.; Qu, M.; Chuang, C.A.; Xiong, L.; Nabaa, A.; Young, Z.A.; Ren, Y.; Kenesei, P.; Zhang, F.; Chen, L. Phase Transformation Dynamics Guided Alloy Development for Additive Manufacturing. *Addit. Manuf.* **2022**, *59*, 103068. [CrossRef]
11. Wen, T.; Li, Z.; Wang, J.; Yang, F.; Zhu, M.; Luo, Y.; Zhang, L.; Liu, Z.; Qiu, D.; Yang, H.; et al. CALPHAD Aided Design of a Crack-Free Al-Mg-Si-Ti Alloy with High Strength: Heterogeneous Nucleation and Eutectic Filling during Additive Manufacturing. *Virtual Phys. Prototyp.* **2024**, *19*, e2378930. [CrossRef]
12. Liu, Z.; Zhou, Q.; Liang, X.; Wang, X.; Li, G.; Vanmeensel, K.; Xie, J. Alloy Design for Laser Powder Bed Fusion Additive Manufacturing: A Critical Review. *Int. J. Extrem. Manuf.* **2024**, *6*, 022002. [CrossRef]
13. Attallah, M.M.; Jennings, R.; Wang, X.; Carter, L.N. Additive Manufacturing of Ni-Based Superalloys: The Outstanding Issues. *MRS Bull.* **2016**, *41*, 758–764. [CrossRef]
14. Vogelpoth, A.; Saewe, J.; Krull, H.-G.; Richert, S.; Weiland, P.; Nerzak, T.; Eibl, F.; Pastors, F. Additive Manufacturing of Tool Steels. *Steel Res. Int.* **2023**, *94*, 2200372. [CrossRef]
15. Galbusera, F.; Demir, A.G.; Platl, J.; Turk, C.; Schnitzer, R.; Previtali, B. Processability and Cracking Behaviour of Novel High-Alloyed Tool Steels Processed by Laser Powder Bed Fusion. *J. Mater. Process. Technol.* **2022**, *302*, 117435. [CrossRef]
16. Zong, H.; Kang, N.; El Mansori, M. Laser Powder Bed Fusion Additive Manufacturing of High-Strength Hot Tool Steel via in-Situ Heat Treatment Induced Nano-Scaled Strengthening Mechanism. *Nano Mater. Sci.* 2025, *in press*. [CrossRef]
17. Böhler Ampo W360 Datasheet. Available online: https://www.bohler.fr/app/uploads/sites/248/productdb/api/st036en_additive-manufacturing-powder.pdf (accessed on 22 April 2026).
18. Wang, H.; Zhang, M.; Sun, R.; Cui, S.; Mo, J. Performance Improvement Strategy of the TBM Disc Cutter Ring Material and Evaluation of Impact-Sliding Friction and Wear Performance. *Wear* **2023**, *526–527*, 204943. [CrossRef]
19. Hawryluk, M.; Lachowicz, M.; Zwierzchowski, M.; Janik, M.; Gronostajski, Z.; Filipiak, J. Influence of the Grade of Hot Work Tool Steels and Its Microstructural Features on the Durability of Punches Used in the Closed Die Precision Forging of Valve Forgings Made of Nickel-Chrome Steel. *Wear* **2023**, *528–529*, 204963. [CrossRef]
20. Fällgren, C.; Beier, T.; Vormwald, M.; Kleemann, A. Autofrettage of High-Pressure Components Made of Ultra-High-Strength-Steel. *Procedia Struct. Integr.* **2022**, *37*, 948–955. [CrossRef]
21. Hawryluk, M.; Ziemba, J.; Zwierzchowski, M.; Janik, M. Analysis of a Forging Die Wear by 3D Reverse Scanning Combined with SEM and Hardness Tests. *Wear* **2021**, *476*, 203749. [CrossRef]
22. Wróbel, J.; Kulawik, A.; Bokota, A. The Numerical Analysis of the Hardening Phenomena of the Hot-Work Tool Steel. *Procedia Eng.* **2017**, *177*, 33–40. [CrossRef]
23. Zanni, M.; Di Egidio, G.; Tonelli, L.; Morri, A.; Ceschini, L. An Analysis of the Influence of Heat Treatments and Surface Finishing Conditions on the High Cycle Fatigue Behaviour of W360 Hot Work Tool Steel Produced by Powder Bed Fusion—Laser Beam. *Mater. Sci. Eng. A* **2025**, *932*, 148237. [CrossRef]
24. Zanni, M.; Berto, F.; Vullum, P.E.; Tonelli, L.; Morri, A.; Ceschini, L. Effect of Heat Treatment and Defects on the Tensile Behavior of a Hot Work Tool Steel Manufactured by Laser Powder Bed Fusion. *Fatigue Fract. Eng. Mater. Struct.* **2023**, *46*, 2681–2696. [CrossRef]
25. Zanni, M.; Morri, A.; Messieri, S.; Ceschini, L. Tensile Behaviour of a Hot Work Tool Steel Manufactured via Laser Powder Bed Fusion: Effect of an Innovative High Pressure Heat Treatment. *Procedia Struct. Integr.* **2023**, *47*, 370–382. [CrossRef]
26. Vinčić, J.; Aversa, A.; Lombardi, M.; Manfredi, D. Processability and Microstructural Evolution of W360 Hot Work Tool Steel by Directed Energy Deposition. *Met. Mater. Int.* **2024**, *30*, 501–516. [CrossRef]
27. Additool Report on Material for MAM. Available online: https://www.additool.eu/ (accessed on 22 April 2026).
28. Schindelin, J.; Arganda-Carreras, I.; Frise, E.; Kaynig, V.; Longair, M.; Pietzsch, T.; Preibisch, S.; Rueden, C.; Saalfeld, S.; Schmid, B.; et al. Fiji: An Open-Source Platform for Biological-Image Analysis. *Nat. Methods* **2012**, *9*, 676–682. [CrossRef] [PubMed]

29. Wright, J.; Vaughan, G.B.M.; Fitch, A. Merging Data from a Multi-Detector Continuous Scanning Powder Diffraction System. *Comm. Crystallogr. Comput.* **2003**, *1*, 92.
30. Hodeau, J.-L.; Bordet, P.; Anne, M.; Prat, A.; Fitch, A.N.; Dooryhee, E.; Vaughan, G.; Freund, A.K. Nine-Crystal Multianalyzer Stage for High-Resolution Powder Diffraction between 6 keV and 40 keV. In *Proceedings of the Crystal and Multilayer Optics*; SPIE: Bellingham, WA, USA, 1998; Volume 3448, pp. 353–361.
31. Fitch, A.; Dejoie, C.; Covacci, E.; Confalonieri, G.; Grendal, O.; Claustre, L.; Guillou, P.; Kieffer, J.; de Nolf, W.; Petitdemange, S.; et al. ID22—The High-Resolution Powder-Diffraction Beamline at ESRF. *J. Synchrotron Radiat.* **2023**, *30*, 1003–1012. [CrossRef] [PubMed]
32. Du Plessis, A. Effects of Process Parameters on Porosity in Laser Powder Bed Fusion Revealed by X-Ray Tomography. *Addit. Manuf.* **2019**, *30*, 100871. [CrossRef]
33. Ji, W.; Liu, C.; Dai, S.; Deng, R. Microstructure, Properties and Crack Suppression Mechanism of High-Speed Steel Fabricated by Selective Laser Melting at Different Process Parameters. *Chin. J. Mech. Eng.* **2023**, *36*, 46. [CrossRef]
34. Saewe, J.; Gayer, C.; Vogelpoth, A.; Schleifenbaum, J.H. Feasability Investigation for Laser Powder Bed Fusion of High-Speed Steel AISI M50 with Base Preheating System. *Berg. Huettenmaenn. Monatshefte* **2019**, *164*, 101–107. [CrossRef]
35. Qin, S.; Herzog, S.; Kaletsch, A.; Broeckmann, C. Effects of Pressure on Microstructure and Residual Stresses during Hot Isostatic Pressing Post Treatment of AISI M50 Produced by Laser Powder-Bed Fusion. *Metals* **2021**, *11*, 596. [CrossRef]
36. Scime, L.; Beuth, J. Melt Pool Geometry and Morphology Variability for the Inconel 718 Alloy in a Laser Powder Bed Fusion Additive Manufacturing Process. *Addit. Manuf.* **2019**, *29*, 100830. [CrossRef]
37. Kunz, J.; Saewe, J.; Herzog, S.; Kaletsch, A.; Schleifenbaum, J.H.; Broeckmann, C. Mechanical Properties of High-Speed Steel AISI M50 Produced by Laser Powder Bed Fusion. *Steel Res. Int.* **2020**, *91*, 1900562. [CrossRef]
38. Zhang, H.; Hou, J.; Liu, X.; Sun, D.; Zhu, Y.; Hao, M.; Zhang, K.; Huang, A.; Tian, X. Martensitic Steels via Laser Powder-Based Additive Manufacturing: Recent Advances in Process Parameters, Microstructure Tailoring, and Mechanical Performance. *Mater. Des.* **2025**, *258*, 114574. [CrossRef]
39. Alnajjar, M.; Christien, F.; Wolski, K.; Bosch, C. Evidence of Austenite By-Passing in a Stainless Steel Obtained from Laser Melting Additive Manufacturing. *Addit. Manuf.* **2019**, *25*, 187–195. [CrossRef]
40. Lashgari, H.R.; Adabifiroozjaei, E.; Kong, C.; Molina-Luna, L.; Li, S. Heat Treatment Response of Additively Manufactured 17-4PH Stainless Steel. *Mater. Charact.* **2023**, *197*, 112661. [CrossRef]
41. Wang, J.; Liu, S.; Fang, Y.; He, Z. A Short Review on Selective Laser Melting of H13 Steel. *Int. J. Adv. Manuf. Technol.* **2020**, *108*, 2453–2466. [CrossRef]
42. Kim, S.-H.; Jeong, S.G.; Son, D.M.; Kim, H.S.; Kim, S.-J. Intrinsic Brittleness of Laser Powder Bed Fusion Processed H13 Hot Work Tool Steel. *Addit. Manuf.* **2024**, *96*, 104564. [CrossRef]
43. Huang, Y.; Fleming, T.G.; Clark, S.J.; Marussi, S.; Fezzaa, K.; Thiyagalingam, J.; Leung, C.L.A.; Lee, P.D. Keyhole Fluctuation and Pore Formation Mechanisms during Laser Powder Bed Fusion Additive Manufacturing. *Nat. Commun.* **2022**, *13*, 1170. [CrossRef] [PubMed]
44. Quintino, L.; Assunção, E. Conduction Laser Welding. In *Handbook of Laser Welding Technologies*; Elsevier: Amsterdam, The Netherlands, 2013; pp. 139–162.
45. Huang, J.; Li, M.; Wang, H.; Ma, S.; Zhang, J.; Wang, C.; Liu, Q. Investigation of Local Cooling Rate and Microsegregation Behavior in Low-Carbon Steel During Thin Slabs Continuous Casting Process. *Steel Res. Int.* **2026**, *early view*. [CrossRef]

Disclaimer/Publisher's Note: The statements, opinions and data contained in all publications are solely those of the individual author(s) and contributor(s) and not of MDPI and/or the editor(s). MDPI and/or the editor(s) disclaim responsibility for any injury to people or property resulting from any ideas, methods, instructions or products referred to in the content.